Draft version February 18, 2026
Typeset using LaTeX default style in AASTeX63

Synoptic Maps of Solar Magnetic Field and Open Magnetic Flux

Yang Liu,[1] C. Nick Arge,[2] Shaela I.Jones,[2,3] Andrew Leisner,[4] Ruizhu Chen,[1] and J. Todd Hoeksema[1]

[1] *W. W. Hansen Experimental Physics Laboratory, Stanford University, Stanford, CA 94305-4085, USA*
[2] *NASA Goddard Space Flight Center, Code 670, Greenbelt, MD 20771, USA*
[3] *Catholic University of America, 620 Michigan Avenue, N.E. Washington, DC 20064, USA*
[4] *George Mason University, Fairfax, VA, USA*

ABSTRACT

The interplanetary magnetic field (IMF) measured near Earth can be up to two times greater than that derived from models using remote solar observations. We investigate this discrepancy by modeling the IMF using a Potential Field Source Surface (PFSS) model using synoptic maps of photospheric magnetic field from May 2010 to April 2024. Five types of radial field synoptic maps are used in this work: the B_r synoptic maps from vector magnetic field data, the M_r synoptic maps from the line-of-sight field data, the rescaled M_r synoptic maps rescaled from the M_r maps by a center-to-limb distance dependent rescaling factor of B_r/M_r, and composite and rescaled composite synoptic maps comprised of a combination of strong-field pixels from the B_r maps and the rest from either the original M_r or rescaled M_r maps. The modeled IMFs from all five types of synoptic maps agree with each other well in solar maximum phase, when they are about two times smaller than in situ measurements. The IMF calculated from the B_r and both composite and rescaled composite synoptic maps matches well with in situ observations during solar minimum from 2017 to 2022. The IMF values modeled from both the M_r and rescaled M_r synoptic maps are still significantly smaller in this time interval. This suggests that (1) the B_r maps represent the radial field better than the M_r; and (2) the PFSS model is appropriate to model the heliospheric magnetic field in solar minimum but has limitations when used near solar maximum.

Keywords: Sun: Magnetic Field; Sun: Interplanetary Magnetic Field; Sun: Open Magnetic Flux

1. INTRODUCTION

Knowledge of the interplanetary magnetic field (IMF) is a key parameter used in space weather forecasts. The IMF is formed as the solar wind flows outward from the Sun into the heliosphere. The strength and orientation of the IMF are deemed to be one of the main drivers to couple solar wind and magnetosphere (Hui & Vichare 2021). However, estimates of the IMF using models of the solar magnetic field can be up to two times smaller than that derived using in situ measurement from spacecraft at 1 AU (see, e.g., Wang & Sheeley 1995; Linker et al. 2017). This discrepancy is often referred to as the "open flux problem."

The IMF is typically determined using either a Potential Field Source Surface (PFSS) or a Magnetohydrodynamic (MHD) coronal model using global maps of the radial photospheric magnetic field as its input (Wang & Sheeley 1995; Linker et al. 2017). PFSS models assume that the magnetic field is potential in a region between the solar surface and a so-called source surface, where the magnetic is forced to be purely radial and open (Schatten et al. 1969; Altschuler & Newkirk 1969) at and beyond it. The source surface is typically set to be at 2.5 solar radii (2.5 R_s)(see, e.g., Hoeksema et al. 1983). The IMF is then estimated from the total unsigned open magnetic flux as determined from a PFSS or coronal MHD model. The open magnetic flux and thus IMF can also be estimated by overlaying coronal holes derived from EUV or Helium 10830 observations onto synoptic maps of the surface magnetic field (Linker et al. 2017, 2021; Wallace et al. 2019; Heinemann et al. 2024; Arge et al. 2024), where it is assumed that the magnetic field in the coronal holes opens up to the interplanetary space. Although the IMF modeled from both approaches agree very well

Corresponding author: Yang Liu
yliu@sun.stanford.edu

each other (Linker et al. 2017; Wallace et al. 2019), they can be up 2 times too small compared to that derived from in situ observations at 1 AU.

Several different approaches have been explored to address the discrepancies found between in situ measurement and modeled IMF. From the model perspective, adjusting the height of the source surface can increase or decrease the amount of open flux from the PFSS model, but no single fixed source surface height matches in situ observations over time. Further, adjusting the source surface height so that the derived IMF values and the in situ IMF match can result in the sizes of modeled coronal holes differing significantly from observations (Riley et al. 2019). Open flux estimates using direct coronal hole observations overlayed on top of photospheric synoptic maps yield results similar to those obtained from the PFSS model results (Wallace et al. 2019; Linker et al. 2021).

The boundary data used as input to PFSS and MHD models (i.e., diachronic or Carrington maps of the radial magnetic field in the photosphere) are also investigated to address this discrepancy. The synoptic maps derived from various magnetograph instruments have been used in coronal models and the estimates obtained for the IMF at 1 AU have been compared. In all of the cases explored, the resulting estimates of the IMF were found to be substantially different from that derived using in situ observations (Linker et al. 2017). The impact of using synchronic versus diachronic maps of photospheric magnetic field to the modeling results is also explored. The influence appears to be very minor (Wallace et al. 2019). Riley et al. (2019) modified a Carrington synoptic map of the radial field for Carrington Rotation CR 2098 by increasing the polar field by 20% and found that it led to agreement between the modeled IMF from a MHD simulation and observation. However, this test was only done for a single Carrington Rotation during solar minimum when the polar field reaches its maximum. This specific finding is inconsistent with the general result found by Arge et al. (2024) demonstrating that modeled and in situ derived open flux agree best during solar minimum and that the major and sustained discrepancies occur primarily during solar maximum. Modifying the polar field strengths during solar maximum, when the discrepancies between modeled and in situ derived open flux is largest (i.e., as much as a factor of two), is therefore not likely to bring modeled and observed open fluxes in alignment, as the polar fields are the weakest at this time and therefore contribute little to the total open magnetic flux (Arge et al. 2024).

Wang & Sheeley (1995) applied a saturation correction to the synoptic maps of radial magnetic field from Mount Wilson Observatory (MWO) and Wilcox Solar Observatory (WSO). The saturation is derived from observation by Ulrich (1992); Ulrich et al. (2009) specifically for the MWO observation. The IMF derived from these corrected synoptic maps with the PFSS model agrees well with in situ observations. Wang et al. (2022) further argue that the MWO's magnetograms need to be corrected for this saturation. While this saturation correction is successful in terms of modeling the IMF, it remains to be tested whether it is also reasonable to apply to magnetograms taken by other instruments, especially the vector magnetograms taken by the *Solar Dynamics Observatory*'s (SDO; Pesnell et al. 2012) *Helioseismic and Magnetic Imager* (HMI; Scherrer et al. 2012) or by the Vector Spectromagnetograph instrument (VSM) on the *Synoptic Optical Long-term Investigations of the Sun* (SOLIS) telescope (Keller et al. 2003) because their measurements and data processing are totally different from MWO's. In a comparison study conducted for a single Carrington rotation, Linker et al. (2017) found synoptic maps constructed from magnetograms from other instruments, including HMI vector magnetograms, and used as input to a PFSS model produced IMF values that are much lower than those derived from 1 AU in situ observations.

While the boundary data are intensively studied, one issue has not been well addressed in previous studies: the true radial field in the synoptic maps. In general, the coronal models used to make estimates of total open unsigned magnetic flux make use of global maps of the radial component of photospheric magnetic field. For all of the studies, the input maps used have been radial field synoptic maps produced from the line-of-sight magnetic field measurement, except only one case study that makes use of the HMI vector magnetograms for one Carrington Rotation (Linker et al. 2017). The radial field in those synoptic maps is computed from the corresponding line-of-sight magnetograms with an assumption that the field is radial. Vector magnetic field data can certainly provide the true radial component of magnetic field with minimal assumptions. With the routine observation of the full-disk vector magnetic field taken by the HMI now available for 15 years, it is timely to investigate how the true radial field synoptic maps impact modeling of the IMF. This is the purpose of this study.

The paper is organized as follows. Section 2 describes the methodology. The synoptic maps of radial magnetic field are described in Section 3. We present the results in Section 4. The paper is concluded in Section 5.

2. METHODOLOGY

Similar to many previous studies (see, e.g., Wang & Sheeley 1995; Linker et al. 2017), we apply the PFSS model to the synoptic maps of magnetic field to calculate the open magnetic flux. In this study, the source surface is set to be at 2.5 solar radii. The total open magnetic flux is obtained by calculating the unsigned flux at the source surface from the PFSS result and then the magnitude of the field is estimated at 1 AU (i.e., at $\sim$ 215 solar radii) by multiplying this value by $(2.5/215)^2$.

We make use of various types of synoptic maps of the radial magnetic field to calculate the open flux. The data used are from HMI observations. In Section 3, we describe in detail the maps of different types.

3. DATA

HMI routinely produces Carrington synoptic charts of radial magnetic field from the full-disk line-of-sight magnetograms (M_r synoptic charts hereafter) and the full-disk vector magnetograms (B_r synoptic charts hereafter). These synoptic charts are provided to the community through the Joint Science Operations Center (JSOC) at Stanford through $http://jsoc.stanford.edu$. A detailed description of these two types of synoptic charts is given in Section 3.1. For this study, we also produce three additional types of synoptic charts for test. The "rescaled M_r synoptic chart" is described in Section 3.2 and two types of "composite synoptic charts" in Section 3.3.

3.1. *Synoptic Maps of Radial Magnetic Field from the JSOC*

3.1.1. *The M_r Synoptic Charts*

The M_r synoptic charts are produced from the full-disk line-of-sight magnetograms observed at a cadence of 720 seconds. First, the HMI 720-second line-of-sight magnetograms are remapped to a Carrington coordinate grid. Each point in the grid has been adjusted to the time of its central meridian crossing in order to minimize additional smearing when carrying out averaging attribute to the differential rotation, as suggested by Ulrich et al. (2002). Then the line-of-sight field is converted to radial field by dividing by cosine of the center-to-limb angle, assuming that the field is purely radial. Initially, the remapped grid retains the spatial resolution of the disk-center pixel, i.e., 0.03°. It reduces to 0.1° by convolving a two-dimensional Gaussian function. The width of the Gaussian is three pixels. The field strength measured at each synoptic grid point is averaged from all of the contributing remapped magnetograms. Currently the average is done with the measurements from the twenty 720-second magnetograms that contribute pixels observed closest to the central meridian. Outliers are excluded if their values depart from the median by more than three times that of the Root Mean Square (RMS). If it happens, pixels next closest to the central meridian are added. The effective temporal width of the HMI synoptic-map contribution is about four hours at each Carrington longitude, i.e. within two hours of central meridian passage. This means that the pixels used are roughly within ±1.2° of central meridian.

3.1.2. *B_r Synoptic Charts*

B_r synoptic charts are produced using a similar scheme as the M_r charts except the radial field B_r is obtained directly from the measurement of vector magnetic field. A detailed description for HMI synoptic charts of vector magnetic field can be found in Liu et al. (2017).

3.2. *Rescaled Synoptic Maps of Radial Magnetic Field*

3.2.1. *B_r/M_r Ratio*

The radial field M_r computed from the line-of-sight field may depart from the true radial field B_r, the difference can be pronounced where the field is not primarily radial, such as in strong field regions. We determine this difference using HMI full-disk vector magnetograms.

First, we choose HMI full-disk vector magnetograms (series name is $hmi.B\_720s$) in 2011 at a cadence of one hour. In total more than 8000 magnetograms are selected. For each vector magnetic field datum, we choose B_r (true radial field) from the vector field data and M_r (the calculated line-of-sight field) determined from the same vector data by $M_r = B \times cos(\theta)/cos(\rho)$, assuming the magnetic field is radial. $B \times cos\theta$ is the line-of-sight field, where B is field strength and θ is inclination. ρ is center-to-limb angle. Then, both B_r and M_r are rebind from their original size of 4096×4096 to 512×512. This way, there are about 8000 pairs of B_r and M_r for each point on the solar disk. For each point, we calculate the ratio B_r/M_r from each pair of data, excluding the pairs where the field strength is less than a threshold or B_r and M_r have opposite signs. The threshold depends on the center-to-limb distance, as shown in Fig. 1. A description of how to derive the threshold is given in next paragraph. The median of B_r/M_r ratio from

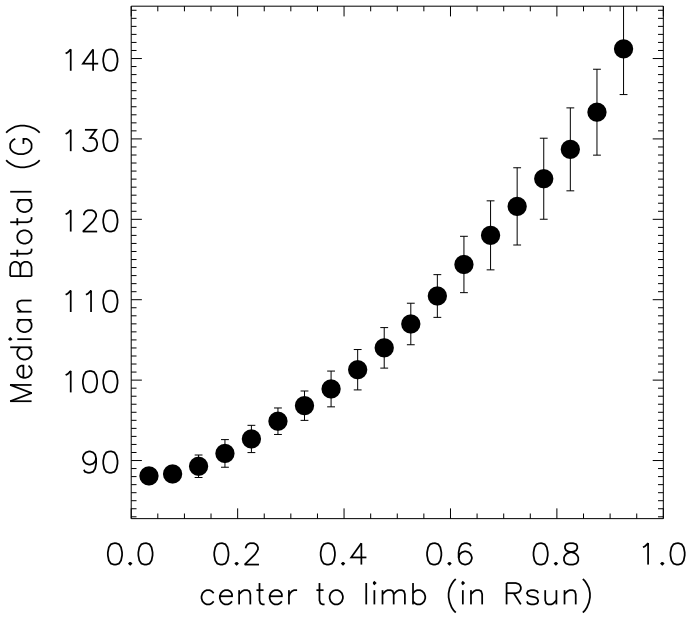

Figure 1. Median of field strength as a function of center-to-limb distance derived from 709 full-disk vector magnetograms in 2011.

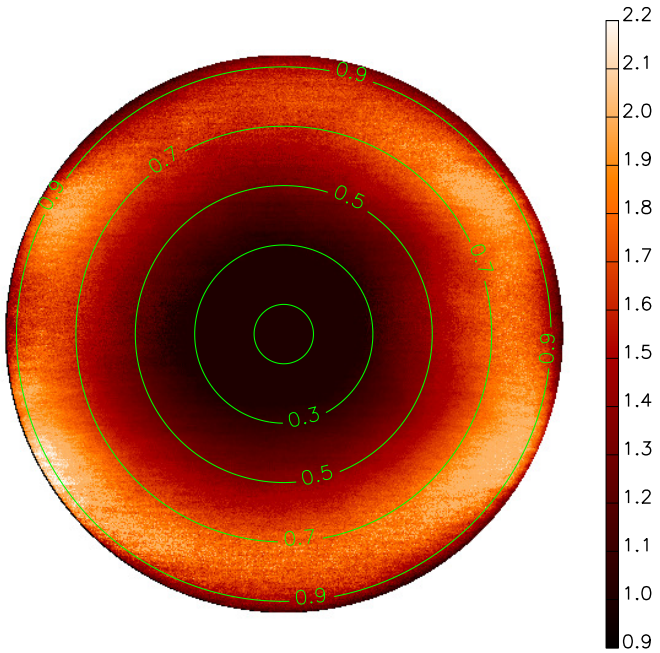

Figure 2. Ratio of B_r/M_r over the Sun's disk derived from more than 8000 individual full-disk vector magnetograms taken in 2011. Green circles refer to the distances to the disk center. See the text for more details.

the selected pixels is chosen as the B_r/M_r ratio for this point. This procedure is repeated over the entire solar disk, and finally, a mask of B_r/M_r is obtained. This mask is shown in Figure 2.

The threshold of the field strength shown in Fig 1 is derived from 709 full disk vector magnetograms in 2011. The data are taken at 06:00 UT and 18:00 UT each day when the orbital velocity of the satellite reaches its minimum. Firstly, we re-binned the magnetograms from 4096×4096 to 512×512. Then we divided the solar disk into concentric annuli, each with 0.05 solar radii wide, and pooled the pixels within each annulus from all 709 full-disk vector-field maps. For every annulus we calculated the median field strength and its standard deviation. Since many pixels sample quiet-Sun regions where the magnetic field is very weak and magnetic signal is below the noise level, the median of the

measured field strength is deemed to be the noise level. Fig. 1 shows this median which depends on the distance from the center to the limb. This curve is used as a threshold to select the data for calculation of the B_r/M_r described in the previous paragraph.

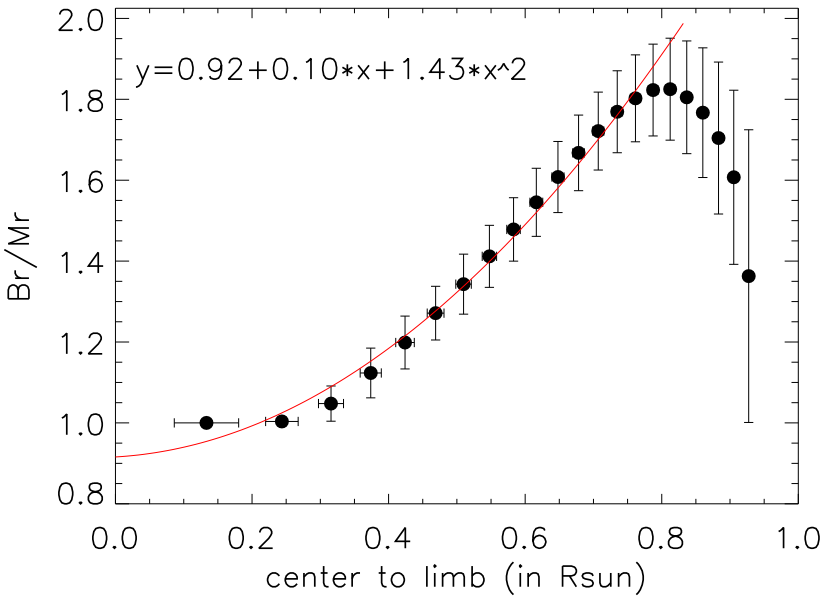

Figure 3. B_r/M_r as a function of the distance to the disk center derived from the data of the rescaling ratio mask shown in Figure 2 by dividing the mask into annuli with a width that ensure that the total number of pixels in each annulus remains the same. B_r/M_r is an average of the data in each annulus. The error bar refers to the rms of the average in the annulus. The red curve represents an 2-order polynomial ($y = 0.92 + 0.10x + 1.43x^2$) that fits the data points within $0.8Rs$.

The B_r/M_r mask (see Fig. 2) is further divided into annuli such that each annulus contains an equal number of pixels. For each annulus, we calculate the average of B_r/M_r and its standard deviation (σ), as listed in Table 1. The average in each annulus is shown in Figure 3. The error bar represents one σ.

3.2.2. *Numerical Test of The B_r/M_r*

We carry out numerical experiments to test the observational results in previous Section (see Fig. 3) that show (1) B_r is generally greater than M_r; and (2) the ratio depends on the center-to-limb distance.

We assume that distribution of the angle between solar magnetic field and local radial direction on solar surface is a Gaussian function, with its peak at zero degrees. This implies that the magnetic field tends to be radial. With this distribution, we can estimate the ratio B_r/M_r in a statistical manner. Shown in Fig. 4 are the test results, overplotted in red diamonds by the measured B_r/M_r. The black curve in the left panel represents the B_r/M_r estimated by an angle distribution modeled by a Gaussian function with a Full Width at Half Maximum (FWHM) of 85°. The shapes of the curves are qualitatively similar: it starts near unity, gradually increases with the center-to-limb distance, reaches a maximum around $0.8Rs$, and then decreases rapidly toward the limb. This indicates that the numerical model reproduces the variation of B_r/M_r with the center-to-limb distance, as revealed by observation. When the FWHM of the Gaussian function changes, the general pattern still remains – the ratio increases initially and then decreases as the center-to-limb distance increases. But the peak of the curves shifts toward the limb when the FWHM decreases, as shown in the right panel of Fig. 4. The FWHM spans from 0.1π (blue curve) to 10π (red curve), which is roughly equivalent to a uniform distribution.

These tests indicate that M_r is generally underestimated, and this underestimation becomes increasingly severe toward the limb. The effect worsens when the magnetic field deviates more frequently from the radial direction. The presence of seething horizontal magnetic fields in quiet-Sun regions (Harvey et al. 2007) may contribute to enhancing this underestimate because it would increase the FWHM of the angle distribution.

The discrepancy of B_r/M_r between the models and observations as shown in the left panel of Fig. 4 may be due to mismatch between the noise levels of the line-of-sight and transverse magnetic fields. The angle distribution not being a perfect Gaussian function may be another factor. The constant filling factor over the Sun's disk in HMI

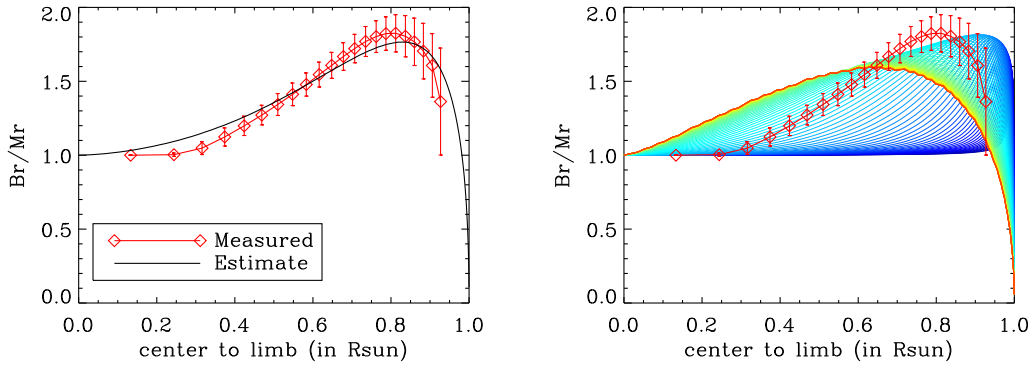

Figure 4. Left: The ratio of B_r/M_r as a function of center-to-limb distance from a numerical simulation in black and observations in red diamonds. The FWHM for this experiment is 85°. Right: B_r/M_r as a function of center-to-limb distance from various simulations with different FWHM of the Gaussian functions in rainbow. Overplotted with red diamonds is the B_r/M_r measured from data. The range of FWHM is from 0.1π (blue curve) to 10π (red curve), effectively approaching a uniform distribution.

inversion processing for the vector magnetic field data also contributes to this discrepancy because the transverse field is over-estimated while the line-of-sight field is under-estimated (Griñón-Marín et al. 2021; Liu et al. 2022). These effects need further investigation.

3.2.3. *Producing Rescaled Synoptic Maps of Radial Magnetic Field*

We use the scaling factor shown in Fig. 3 to rescale the original M_r synoptic maps. The scaling factor first is modeled with a second-order polynomial ($y = 0.92 + 0.10x + 1.43x^2$) that fits the data points within $0.8R_s$, as shown by the red curve in Fig 3; and a spline interpolation is applied to the rest of the data points beyond $0.8R_s$. This scaling factor curve is then applied to the M_r synoptic charts to produce the rescaled M_r synoptic charts. The solar B angle is also taken into account when the rescaling curve is applied. The polar region above 75° in latitude is filled in using a two dimensional function that fits the low latitude observational data. The two dimensional fitting function is a Chebyshev polynomial of the first kind with an order of 5.

3.3. *Composite Maps of Radial Magnetic Field*

A composite synoptic chart of radial magnetic field is produced by combining the corresponding B_r and M_r (or rescaled M_r) synoptic charts. The strong field regions in the composite chart are from the B_r chart, while the remaining areas are from the M_r (or the rescaled M_r) chart. Thus, a composite chart takes advantage of better measurements of the radial field from the B_r chart in strong field regions while avoiding the much noisier data in the quiet Sun regions. This method was previously used by Bertello et al. (2018).

To produce a composite synoptic chart of the radial field, we first make a strong field mask of a synoptic chart. We choose the pixels from the B_r synoptic chart where $|B_r|$ is greater than 135 G, which is $600/\sqrt{20}$. 600 G is about 6 σ of HMI vector field data (Hoeksema et al. 2014), while the value at each pixel in an HMI synoptic chart is usually an average of 20 individual magnetograms. These pixels are set to be 1 in the strong field mask and rest are 0. Then this mask is expanded by dilating it with a 31×31 structuring element. The composite synoptic chart is then produced by combining the non-zero pixels of the strong field mask from the B_r synoptic chart and the zero-value pixels from the M_r (or the rescaled M_r) synoptic chart. This results in two types of composite synoptic charts: the composite charts computed from B_r and M_r (composite synoptic charts hereafter) and the composite charts computed from B_r and rescaled M_r (rescaled composite synoptic charts hereafter).

As an example, we show in Figure 5 how composite radial field synoptic charts of Carrington Rotation 2211 (CR 2211, left panels) and CR 2278 (right) are produced. The top two panels show the rescaled M_r and B_r synoptic charts. The third row shows strong-field masks produced from the B_r charts. The white patches in the chart refer to non-zero (strong field) pixels, and rest are zero-value pixels. The bottom panels are the rescaled composite synoptic charts of radial field from the B_r and the rescaled M_r synoptic charts. CR 2211 is in solar minimum and CR 2278 in solar

Table 1. Ratio of B_r/M_r as a function of center-to-limb distance from HMI vector magnetic field data.

center-to-limb distance (in R_s)	Br/Mr
0.133	1.00000 ± 0.00000
0.244	1.00359 ± 0.01113
0.316	1.04775 ± 0.04352
0.374	1.12340 ± 0.06150
0.424	1.19872 ± 0.06534
0.469	1.27135 ± 0.06638
0.510	1.34302 ± 0.07420
0.548	1.41181 ± 0.07669
0.583	1.47830 ± 0.07843
0.616	1.54537 ± 0.08416
0.648	1.60789 ± 0.08789
0.678	1.66757 ± 0.09345
0.707	1.72146 ± 0.09634
0.735	1.76926 ± 0.10133
0.762	1.80242 ± 0.10745
0.787	1.82291 ± 0.11349
0.812	1.82505 ± 0.12601
0.837	1.80495 ± 0.13935
0.860	1.76695 ± 0.16031
0.883	1.70428 ± 0.18781
0.906	1.60728 ± 0.21525
0.927	1.36291 ± 0.36180

maximum. In solar minimum, the contribution of the B_r synoptic map is mostly in polar regions (see the mask on the left). In solar maximum, the contribution from B_r is mostly at lower latitudes in active regions.

4. RESULT

We show a comparison of modeled values of unsigned IMF and the in situ observations in Figure 6. The top panel shows the IMF values from May 2010 to April 2024. The black curve represents the measured IMF at 1 AU, which is the average of the unsigned magnetic strength over each Carrington rotation from the daily averages of the near-Earth B_x from the OMNIWeb site at $http://omniweb.gsfc.nasa.gov$. The curves in other colors refer to the modeled IMF obtained using different synoptic charts of radial field that are applied to the PFSS model to calculate the open flux, as described in Section 2. The red, light green, blue, orange, and dark green curves refer to the modeled IMF from the M_r (see Section 3.1.1), rescaled M_r (see Section 3.2), B_r (Section 3.1.2), composite, and rescaled composite (Section 3.3) Carrington synoptic charts, respectively. The average polar field is shown in the bottom panel. It is obtained by averaging over the area from latitudes 60° to 90° from the HMI M_r magnetograms that are calculated from the HMI line-of-sight magnetograms. Only data taken at 06:00 and 18:00 UT are chosen, when the orbital velocity relative to the Sun reaches its minimum. The vertical dashed lines refer to the times of CR 2211 in solar minimum and CR 2278 in solar maximum, as shown in Figure 5.

In the rising, maximum, and decaying phases of the solar cycle (from 2010 to 2016 and from 2022 to 2024, see the bottom panel of Figure 6), the modeled IMFs from all types of synoptic maps agree with each other fairly well and all are about two times smaller than the in situ measurements. However, around solar minimum, 2017-2021, the modeled IMF from both kinds of composite maps and the B_r synoptic maps match the observations much better. Still, the original M_r (red) IMF remains about two times smaller than the observations though the gap for the rescaled M_r (light green) is smaller.

Figure 6 shows two interesting results. First, during solar minimum, B_r and both types of composite synoptic maps yield IMFs that match observations well, but the modeled IMF from the original and rescaled M_r synoptic maps are still significantly smaller than the observations. The main difference between the two M_r maps (both original and rescaled) and the other maps is that the strong fields in the composite maps are those found in the corresponding

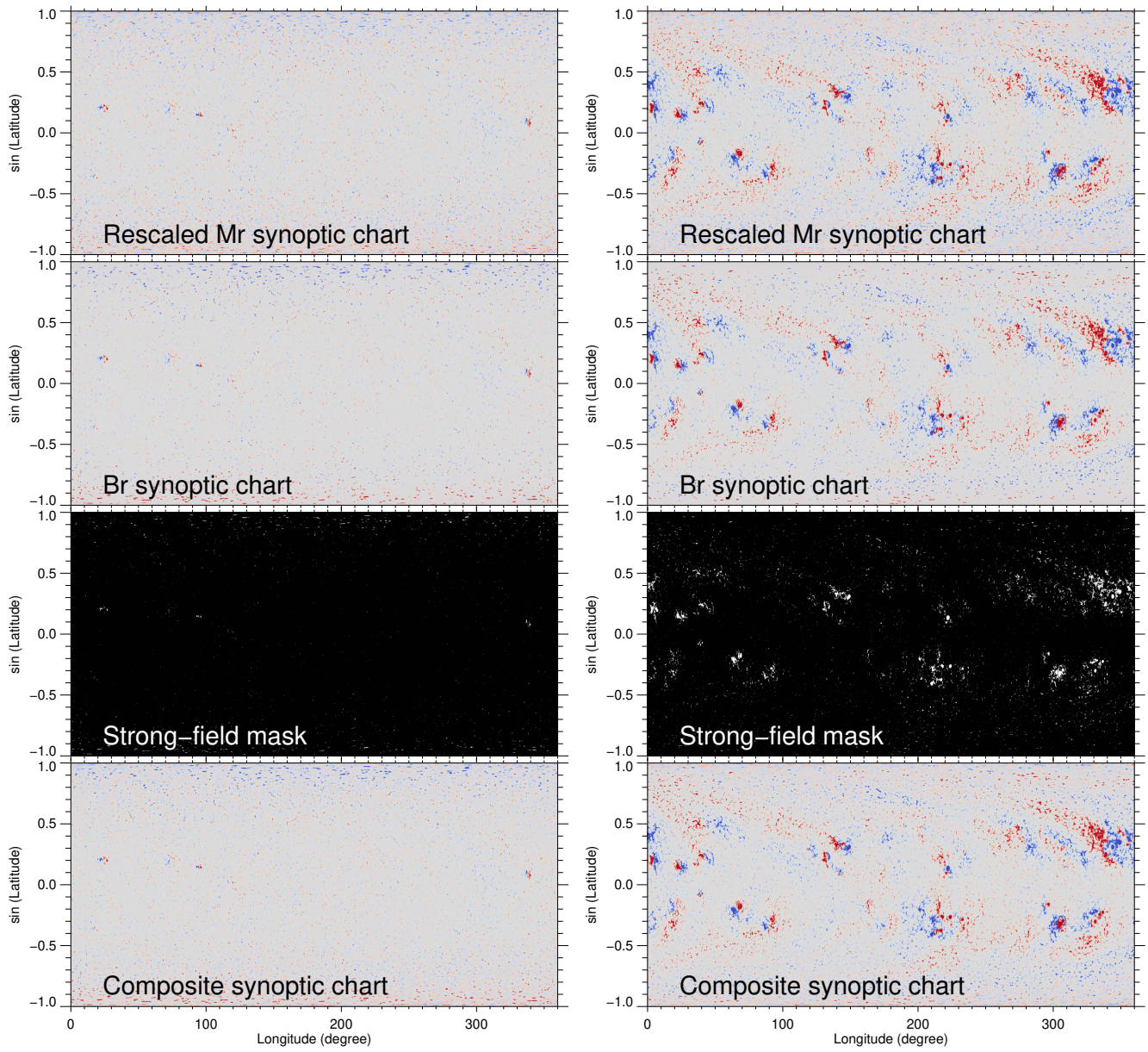

Figure 5. From top to bottom are the rescaled M_r, B_r, strong-field mask, and composite synoptic charts for CR 2211 in solar minimum (left) and CR 2278 in solar maximum (right). For the radial field charts (rows 1, 2, and 4), blue and red refer to positive and negative fields. They are saturated at ±150 G.

B_r maps. In solar minimum, these pixels are mostly at high latitudes, including polar regions (see the left panels of Figure 5). This suggests that (1) B_r provides better radial field than rescaled M_r, especially at high latitudes, which is in accordance with the result that the modeled IMF agrees with observations after increasing the polar field (Riley et al. 2019). And (2) the PFSS model can be used to model the IMF during solar minimum.

Second, all of the different types of synoptic maps produce IMFs that are much smaller than observations during solar maximum. Further, these modeled IMFs agree with each other well, including the one from the B_r synoptic maps. It is much clearer in the time interval of the polar field reversal when the polar field reaches its minimum. During polar field reversal, as seen in the right panels of Figure 5, the B_r maps contribute significantly to the corresponding composite synoptic maps, but those pixels are mostly at low latitudes in active regions and very few pixels are at the polar regions. This implies, as before, that total open flux as obtained using the standard approach with a PFSS

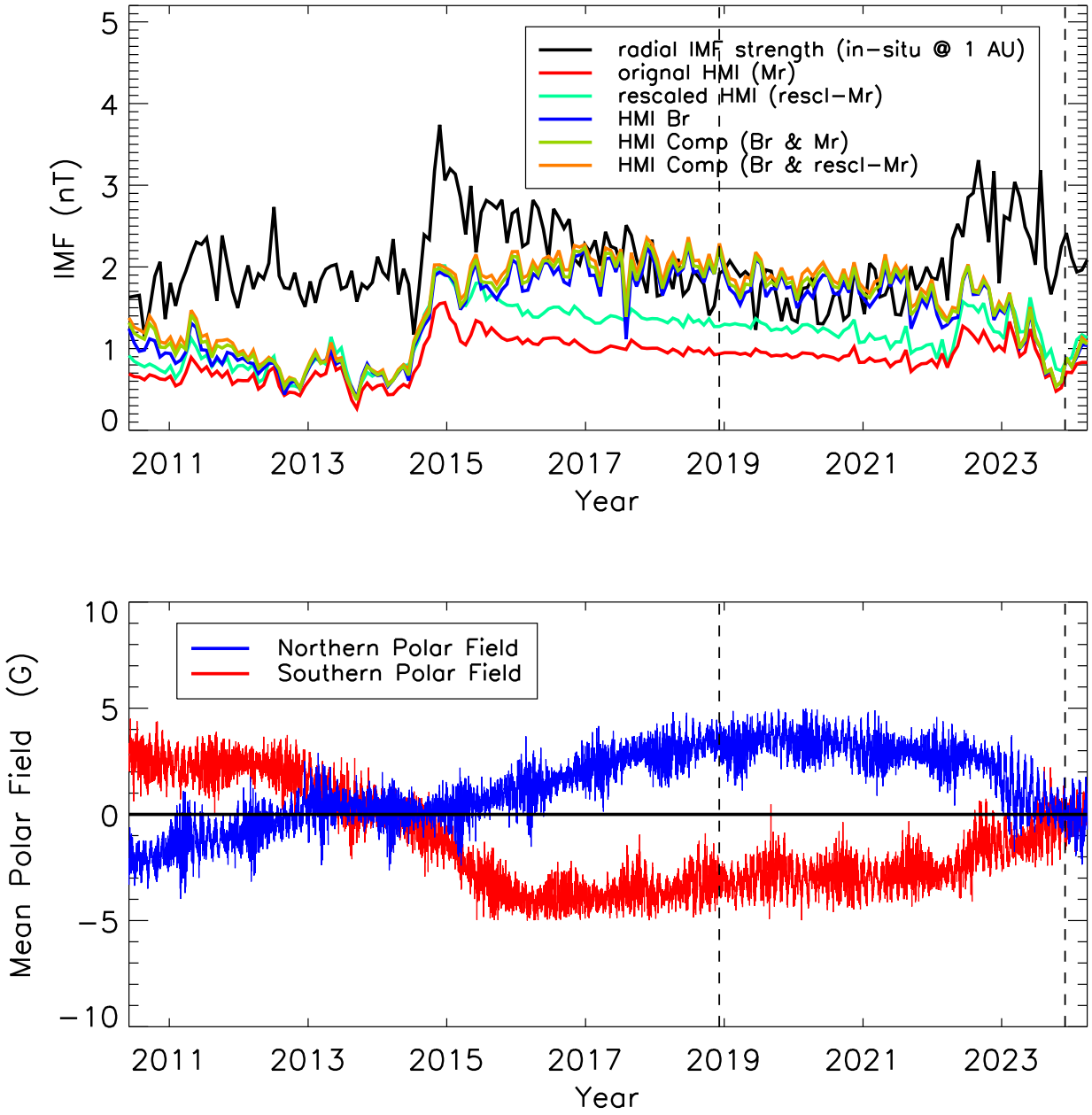

Figure 6. Top: IMF in the time interval between May 2010 and April 2024 from observation (black curve) and from the PFSS model applied to various synoptic maps. Red, light green, blue, orange, and dark green curves represent modeled IMF from M_r, rescaled M_r, B_r, composite, and rescaled composite Carrington synoptic charts, respectively. Bottom: Polar field averaged over the area from latitudes 60° to 90° from the HMI M_r magnetograms that are calculated from the HMI line-of-sight magnetograms. Only data taken at 06:00 and 18:00 UT are used. The orbital velocity relative to the Sun reaches its minimum at these two instances. The vertical dashed lines refer to the times of CRs 2211 and 2278 as shown in Figure 5.

model will not generate results consistent with observations during periods outside solar minimum. However, it has been demonstrated that the missing open flux in solar maximum usually resides at the boundaries of coronal holes or near active regions (Arge et al. 2024).

It is interesting to compare the modeled IMF from the rescaled M_r maps and the rescaled composite synoptic maps. The difference between the two types of maps is that the rescaled composite maps contain B_r data in strong-field regions. Around solar minimum, though, only a small fraction of pixels at high latitudes in the rescaled composite maps comes from B_r (see the left panels in Figure 5) and this yields a significant difference in modeled IMF: The modeled IMF from the rescaled M_r is still much smaller than observations, whereas the IMF from the rescaled

composite maps agrees with the observations. Around solar maximum, however, the modeled IMFs agree with each other although a big faction of area in the rescaled composite maps is contributed by the B_r maps (see the right panels in Figure 5). The modeled IMFs from these two types of maps even agree with that from the original M_r synoptic maps (red curve in Figure 6). This may suggest that in solar maximum, the PFSS model, and perhaps also the MHD simulation (because MHD simulations also leads to the open flux problem in solar maximum, Linker et al. (2017)), is not sufficient to model the open flux without including partially open coronal hole boundary regions. Throughout the rising, maximum, and early declining phases the models all give similar results, even though the boundary data are quite different.

5. DISCUSSION & CONCLUSIONS

We have calculated the IMF using the PFSS model and a variety of radial magnetic field synoptic charts derived from HMI observation from May 2010 to April 2024. Five types of radial field synoptic charts are used in this work: the original M_r synoptic charts that are produced from the line-of-sight magnetograms (see Section 3.1.1), rescaled M_r synoptic charts that are produced from the original M_r synoptic charts rescaled with a center-to-limb dependent scaling factor of B_r/M_r derived from observations (see Section 3.2), B_r synoptic charts constructed directly from the vector field data (Section 3.1.2), and two types of composite synoptic charts that combine B_r with either original M_r synoptic charts or the rescaled M_r synoptic charts (Section 3.3).

The modeled IMFs are then compared with in situ measurements at 1 AU. Around solar minimum the modeled IMF magnitudes from B_r and the two composite synoptic charts (standard and rescaled) agree with observations. The modeled IMF from M_r charts is about two times smaller than observations, while that from the rescaled M_r charts is closer to, but still significantly smaller than, observed IMF. The modeled IMFs from all five types of synoptic charts agree with each other quite well during the rising, maximum, and decay phases of the solar cycle, even though the actual charts of the different types are significantly different from one another. All of them are about two times smaller than the in situ observation outside of solar minimum. This suggests that the PFSS model fails to model the open flux in solar maximum when the polar fields become weak.

Recently Arge et al. (2024) hypothesized a time-dependent partially open boundary of a scale size about one or two supergranules in size bordering the perimeters of coronal holes that contribute additional flux, especially near strong active regions. This boundary is identified in static models such as Wang–Sheeley–Arge model (WSA, Arge & Pizzo 2000; Arge et al. 2003) by tracing field lines at fixed resolution from the outer boundary of the model to the photosphere. When the field lines are backward tracked from the source surface to the solar surface in this manner, they were able to confirm that these boundary regions generate sufficient additional flux to agree with in situ observations spanning a 27-year time interval. As these additional open regions are located mostly at the boundaries of the coronal holes or close to active regions, they appear bright in EUV observation and thus unaccounted for when estimating flux using observationally derived coronal holes.

This model has been tested (Leisner et al. 2024) with these synoptic maps and it has been found that IMF computed from the B_r maps and the rescaled composite synoptic maps agrees with in-situ observation in both solar minimum and maximum. This provides significant evidence to support their approach for estimating total open unsigned magnetic flux and extends the period of agreement with observations for more than 34 years. These results are reported in a paper submitted to ApJ for publication.

ACKNOWLEDGMENTS

We wish to thank the anonymous referee for the valuable comments and suggestions that help improve this work. NASA's SDO satellite and the HMI instrument were joint efforts by many teams and individuals, whose efforts to produce the HMI magnetograms that we analyzed here are greatly appreciated. We acknowledge support from NASA grant 80NSSC22K1016. This work was also partially supported by the NASA DRIVE Science Center COFFIES (Consequence Of Fields and Flows in the Interior and Exterior of the Sun) grant 80NSSC20K0602 and by NASA Contract NAS5-02139 (HMI) to Stanford University.

REFERENCES

Altschuler, M. D., & Newkirk, G. 1969, SoPh, 9, 131, doi: 10.1007/BF00145734

Arge, C. N., Leisner, A., Antiochos, S. K., Wallace, S., & Henney, C. J. 2024, ApJ, 964, 115, doi: 10.3847/1538-4357/ad20e2

Arge, C. N., Odstrcil, D., Pizzo, V. J., & Mayer, L. R. 2003, in American Institute of Physics Conference Series, Vol. 679, Solar Wind Ten, ed. M. Velli, R. Bruno, F. Malara, & B. Bucci (AIP), 190–193, doi: 10.1063/1.1618574

Arge, C. N., & Pizzo, V. J. 2000, J. Geophys. Res., 105, 10465, doi: 10.1029/1999JA000262

Bertello, L., Pevtsov, A. A., & Petrie, G. J. D. 2018, in 2018 Triennial Earth-Sun Summit (TESS), ed. D. Brousseau, 115.02

Griñón-Marín, A. B., Pastor Yabar, A., Liu, Y., Hoeksema, J. T., & Norton, A. 2021, ApJ, 923, 84, doi: 10.3847/1538-4357/ac2aa8

Harvey, J. W., Branston, D., Henney, C. J., Keller, C. U., & SOLIS and GONG Teams. 2007, ApJL, 659, L177, doi: 10.1086/518036

Heinemann, S. G., Owens, M. J., Temmer, M., et al. 2024, ApJ, 965, 151, doi: 10.3847/1538-4357/ad2b69

Hoeksema, J. T., Wilcox, J. M., & Scherrer, P. H. 1983, J. Geophys. Res., 88, 9910, doi: 10.1029/JA088iA12p09910

Hoeksema, J. T., Liu, Y., Hayashi, K., et al. 2014, SoPh, 289, 3483, doi: 10.1007/s11207-014-0516-8

Hui, D., & Vichare, G. 2021, Journal of Geophysical Research (Space Physics), 126, e29270, doi: 10.1029/2021JA029270

Keller, C. U., Harvey, J. W., & Giampapa, M. S. 2003, in Society of Photo-Optical Instrumentation Engineers (SPIE) Conference Series, Vol. 4853, Innovative Telescopes and Instrumentation for Solar Astrophysics, ed. S. L. Keil & S. V. Avakyan, 194–204, doi: 10.1117/12.460373

Leisner, A., Arge, C. N., Antiochos, S. K., Wallace, S., & Henney, C. J. 2024, in AGU Fall Meeting Abstracts, Vol. 2024, SH23F–06

Linker, J. A., Caplan, R. M., Downs, C., et al. 2017, ApJ, 848, 70, doi: 10.3847/1538-4357/aa8a70

Linker, J. A., Heinemann, S. G., Temmer, M., et al. 2021, ApJ, 918, 21, doi: 10.3847/1538-4357/ac090a

Liu, Y., Griñón-Marín, A. B., Hoeksema, J. T., Norton, A. A., & Sun, X. 2022, SoPh, 297, 17, doi: 10.1007/s11207-022-01949-y

Liu, Y., Hoeksema, J. T., Sun, X., & Hayashi, K. 2017, SoPh, 292, 29, doi: 10.1007/s11207-017-1056-9

Pesnell, W. D., Thompson, B. J., & Chamberlin, P. C. 2012, SoPh, 275, 3, doi: 10.1007/s11207-011-9841-3

Riley, P., Linker, J. A., Mikic, Z., et al. 2019, ApJ, 884, 18, doi: 10.3847/1538-4357/ab3a98

Schatten, K. H., Wilcox, J. M., & Ness, N. F. 1969, SoPh, 6, 442, doi: 10.1007/BF00146478

Scherrer, P. H., Schou, J., Bush, R. I., et al. 2012, SoPh, 275, 207, doi: 10.1007/s11207-011-9834-2

Ulrich, R. K. 1992, in Astronomical Society of the Pacific Conference Series, Vol. 26, Cool Stars, Stellar Systems, and the Sun, ed. M. S. Giampapa & J. A. Bookbinder, 265

Ulrich, R. K., Bertello, L., Boyden, J. E., & Webster, L. 2009, SoPh, 255, 53, doi: 10.1007/s11207-008-9302-9

Ulrich, R. K., Evans, S., Boyden, J. E., & Webster, L. 2002, ApJS, 139, 259, doi: 10.1086/337948

Wallace, S., Arge, C. N., Pattichis, M., Hock-Mysliwiec, R. A., & Henney, C. J. 2019, SoPh, 294, 19, doi: 10.1007/s11207-019-1402-1

Wang, Y. M., & Sheeley, N. R., J. 1995, ApJL, 447, L143, doi: 10.1086/309578

Wang, Y. M., Ulrich, R. K., & Harvey, J. W. 2022, ApJ, 926, 113, doi: 10.3847/1538-4357/ac4491